AIAA JOURNAL
Vol. 47, No. 9, September 2009

Numerical Study of Mach 6 Boundary-Layer Stabilization by Means of a Porous Surface

Neil D. Sandham*
University of Southampton, Southampton, England SO17 1BJ, United Kingdom
and
Heinrich Lüdeke†
DLR, German Aerospace Center, 38108 Braunschweig, Germany

DOI: 10.2514/1.43388

Direct numerical simulations are carried out on boundary-layer flow at Mach 6 over a porous surface, in which a Mack mode of instability is excited. The pores are resolved rather than modeled, allowing an evaluation to be made of the accuracy of simplified analytical models used in previous investigations based on linear stability theory. It is shown that the stabilizing effect of porosity is stronger in the simulations than in the corresponding theory for both two- and three-dimensional pores. From comparisons of spanwise grooves, streamwise slots, and square pores, it appears that the detailed surface structure is not as important as the overall porosity, and the hydraulic diameter is able to collapse the results for different pore shapes to good accuracy. When the porous surface consists of fewer larger pores, the flow is noisier, with sound waves generated at the pore edges.

Nomenclature

A	=	amplitude
A_p	=	pore area
C	=	pore circumference
c	=	stretching factor
d	=	pore depth
d_h	=	hydraulic diameter
E	=	internal energy
e	=	internal energy
f, g	=	forcing terms
J_0, J_2	=	Bessel functions of the first kind
k_v, k_t	=	arguments of Bessel functions
$L_{x,y,z}$	=	domain dimensions
M	=	Mach number
N_g	=	number of cells in the pore
n	=	porosity
n_p	=	number of pores
Pr	=	Prandtl number
q	=	heat flux
R	=	gas constant
Re	=	Reynolds number based on boundary-layer displacement thickness
r	=	pore radius
T	=	temperature
t	=	time
u	=	velocity
x, y, z	=	coordinates
Y_1	=	shunt admittance
Z_1	=	series impedance
α, β	=	wave numbers
γ	=	ratio of specific heats
η	=	nondimensional wall-normal coordinate
η_m	=	coordinate of pore bottom
κ	=	thermal conductivity
μ	=	viscosity
ρ	=	density
τ	=	stress tensor
ω	=	complex frequency

Subscripts

i, j	=	directions (1, 2, 3)
rms	=	root mean square
w, aw	=	wall, adiabatic wall

Superscripts

$\bar{}$	=	base flow quantity
$\hat{}$	=	eigenfunction

I. Introduction

WHENEVER transition to turbulence is dominated by the amplification of instability waves, it is natural to ask whether the mechanisms of instability, which may be well known from linear stability theory, can be interfered with by means of changes to the surface boundary conditions, thereby allowing the transition process to be delayed or prevented altogether. Early work in this direction was carried out by Liepmann and Nosenchuck [1], who showed how a Tollmien–Schlichting wave in a flat-plate boundary layer could be canceled by active surface heating. Modern research on this theme is focused on the use of arrays of small-scale actuators that can respond to sensed flow conditions (for an introduction, see Gad-el-Hak [2]). These methods are complex and there is interest in technologically simpler methods, such as the use of a passive porous wall. The modeling of such surfaces for incompressible flow was discussed by Carpenter and Porter [3]. If the technique can be extended to the hypersonic flow regime, there would be a considerable return in terms of the vehicle weight savings. The reduced heat transfer under a laminar boundary layer compared with a turbulent boundary layer means that thermal protection systems could, in principle, be designed to be lighter if transition to turbulence could be delayed. Porous surfaces fabricated from modern ultra-high-temperature ceramic materials represent an attractive passive method of achieving this.

Transition in high-speed flow is dominated by additional modes of instability, known as second (or Mack) modes [4], which are dominant for Mach numbers M above about 4 (and at lower Mach numbers for cooled walls). They are most unstable as two-dimensional waves,

Presented as Paper 1288 at the 47th AIAA Aerospace Sciences Meeting and Exhibit, Orlando, FL, 5 January–5 March 2009; received 22 January 2009; accepted for publication 11 May 2009.

*Professor, School of Engineering Sciences; n.sandham@soton.ac.uk. Senior Member AIAA.

†Research Scientist, Institute for Aerodynamics and Flow Technology; Heinrich.Luedeke@dlr.de. Member AIAA.

whereas at high Mach numbers the first mode of instability is most unstable for oblique wave angles. Thus, the first goal of transition control in high-speed boundary layers is to prevent or delay the growth of Mack modes. Fedorov et al. [5] presented the first linear stability results for porous surfaces, using an analytical model of flow within blind (closed) pores. Their results demonstrated substantial growth-rate reductions for Mack modes, typically by a factor of 2 for porosities of around 0.25 (pore area equal to 25% of the surface area) and 10–20 pores per instability wavelength. The growth rate varied with pore depth, up to depths of around 0.3 boundary-layer displacement thicknesses, after which the growth rate leveled off. The ability of a porous surface to delay transition, at least in some cases, was demonstrated by Rasheed et al. [6] in shock-tunnel experiments of flow over a cone at a nominal Mach number of 5.

Further analysis and experiments were presented in a report by Maslov [7], which confirmed the damping effect of porosity. The effect was found to become stronger as the Knudsen number increased, as modeled by linear theory within the slip flow regime. Fedorov et al. [8] used a different type of surface and demonstrated that similar effects could be achieved with thin porous coatings with a random microstructure. Nonlinear stages of transition were studied by Chokani et al. [9], who found changes in the harmonic and subharmonic resonances and, in particular, the removal of the harmonic resonance, with only marginal destabilization of the first mode. Thus, the passive porous-surface approach appears to be robust to some of the principal determining parameters.

For hypersonic applications, a number of issues remain. On cost grounds, most numerical studies of porous walls have used approximate boundary conditions, of which the Fedorov et al. [5] model is one example, recently extended to Navier–Stokes simulations by Egorov et al. [10]. As far as we are aware, the only two-dimensional numerical simulation studies that resolve the pores are those of Bres et al. [11], which considered acoustic waves impinging on a porous surface, and those of Bres et al. [12], which confirmed the stabilizing effect of porosity. It is still not clear to what extent the linear theory can be trusted for three-dimensional design purposes and different pore configurations. Another issue is that the porous surface may act as a rough surface (for example, if the holes are too big), in a manner that is not fully understood. If this happens, transition may be triggered early and any benefit in reducing the growth rate of Mack modes may be lost. In this paper, we address some of these concerns by running direct numerical simulations that resolve the instability wave and the flow within the pores. The basic methods are validated against linear stability for smooth walls and then a set of two-dimensional simulations of surface with spanwise grooves are run to compare with the linear stability predictions of the effect of porosity. Three-dimensional simulations are used to study the effect of different porous-surface structures. Finally, we consider the effect of wall temperature by two- and three-dimensional simulations of porous surfaces with cold walls.

II. Numerical Methods

Two simulation techniques are used in this work. Direct numerical simulations (DNS) were used to provide complete solutions for flow over and in the pores, and a linear stability code was used as a cheaper prediction method. A temporal formulation, with periodic boundary conditions in the streamwise direction, was chosen for comparison, because this allows an efficient concentration of grid points to resolve multiple pores within one wavelength of the instability. Indeed, the simulations would not be feasible if the spatially developing approach were taken, due to the large computational cost.

A. Direct Numerical Simulation

The equations to be solved are the compressible Navier–Stokes equations for flow of a perfect gas with density ρ, velocity components u_i, pressure p, and internal energy e written in conservation-law form as

$$\frac{\partial \rho}{\partial t} + \frac{\partial \rho u_j}{\partial x_j} = 0 \tag{1}$$

$$\frac{\partial \rho u_i}{\partial t} + \frac{\partial \rho u_i u_j}{\partial x_j} + \frac{\partial p}{\partial x_i} = \frac{\partial \tau_{ij}}{\partial x_j} + f_i \tag{2}$$

$$\frac{\partial \rho E}{\partial t} + \frac{\partial (\rho E + p) u_i}{\partial x_i} = -\frac{\partial q_i}{\partial x_i} + \frac{\partial u_i \tau_{ij}}{\partial x_j} + g \tag{3}$$

where $E = e + u_i u_i/2$. Forcing terms f_i and g are included in the right-hand side of the equations such that a specified parallel base flow $\bar{\rho}(y)$, $\bar{u}_i(y)$, and $\bar{E}(y)$ is time-independent. In practice, these terms are evaluated numerically within the code by computing and storing the initial residual. The base flow and the forcing terms are zero within the pores. This approach means that the laminar base flow is maintained exactly for smooth walls, whereas for porous walls the flow is able to adjust to a local solution of the governing equations. This allows the formation of a small slip velocity when an average streamwise velocity is computed over the wall plane.

The equations are closed with the perfect-gas law:

$$p = \rho R T \tag{4}$$

where R is the gas constant, together with the constitutive relations

$$q_i = -\kappa \frac{\partial T}{\partial x_i} \tag{5}$$

and

$$\tau_{ij} = \mu \left(\frac{\partial u_i}{\partial x_j} + \frac{\partial u_j}{\partial x_i} - \frac{2}{3} \delta_{ij} \frac{\partial u_k}{\partial x_k} \right) \tag{6}$$

The base flow is obtained from a separate solution of the similarity equations for compressible boundary-layer flow, solved by a shooting method. We consider a base flow with Mach number $M = 6$, Reynolds number $Re = 20,000$, Prandtl number $Pr = 0.72$, ratio of specific heats $\gamma = 1.4$, and an adiabatic-wall boundary condition. Viscosity μ is prescribed by Sutherland's law with a constant of 110.4 K and a reference temperature of 216.65 K, leading to a wall temperature of 1522.44 K. The same Sutherland coefficients are used for the thermal conductivity κ. The base profile normal coordinate is normalized by the displacement thickness before being interpolated onto the simulation grid by a cubic spline method.

Calculations in this paper were made with a high-order variant of the DLR, German Aerospace Center FLOWer code. The basic FLOWer code solves the compressible Reynolds-averaged Navier–Stokes equations on block-structured grids with second-order finite volume techniques and cell-centered or cell vertex variables. The high-order version used in the present work [13] uses fourth-order central differencing based on standard compact finite differences in a cell-centered formulation, together with high-order compact filters that are applied at the end of each time step. Options are available for a skew-symmetric splitting of the convective terms and for sponge-zone boundary conditions to reduce reflections. For the present work, we use a sixth-order filter and the standard conservative form of the Euler terms. Time advancement is by a five-step second-order Runge–Kutta method [14]. For the present work, we limit the calculations to rectangular pores so that grids match at the interface, removing interpolation as a possible source of error.

A grid-stretching function is used in all cases that places more points near $y = 0$. Including cases with pores, the function is given by

$$y = L_y \frac{\sinh(c\eta)}{\sinh c} \tag{7}$$

where $\eta_m < \eta < 1$ and c and η_m are chosen iteratively near a target c such that $y(\eta_m) = -d$ (where d is the pore depth) and an integer number of grid cells within the pore.

The calculations use periodic boundary conditions in the x and z directions. The use of a periodic boundary condition in the x direction corresponds to the temporal formulation of linear stability theory.

This approach is supported by [12], in which it was found that spatial and temporal results could be interchanged to good accuracy using the Gaster transformation. A no-slip wall with temperature set to the wall temperature of the base flow is applied at $y = 0$ and on surfaces within the pores. At the outer boundary, characteristic conditions are used.

B. Linear Stability Theory

In the analysis of the linear stability of compressible flows [4], waves are represented as normal modes: for example,

$$\rho = \hat{\rho}(y) \exp[i(\alpha x + \beta z - \omega t)] \tag{8}$$

and similarly for other variables, where α and β are real wave numbers in the temporal stability approach adopted here, and ω is a complex frequency that is the result of the analysis. The imaginary part ω_i gives the disturbance growth rate. A caret over a variable denotes an eigenfunction.

A direct matrix solution method is used for the linear stability system of equations, with derivatives computed with a mapped Chebyshev method using a minimum of 150 collocation points. The code was validated by the comparison with a number of sources in the literature, including Malik [15]. As shown in the Appendix, the solutions for base flows that do not satisfy the Navier–Stokes equations are not unique and vary slightly depending on the method of derivation. The linear stability results presented here are based on a derivation from the conservative equations (1–3). A stability diagram is shown in Fig. 1, plotting the growth rate ω_i against the wave number α. The most unstable mode is the second (Mack) mode, with a maximum amplification rate near $\alpha = 2.1$. The first mode is most unstable as an oblique wave, reaching a growth rate of 0.01347 at $\alpha = 0.53$ and a wave angle of 62 deg.

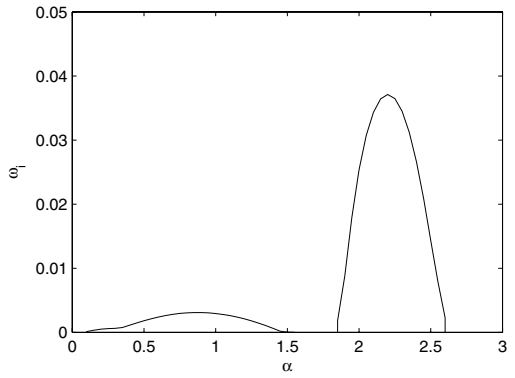

Fig. 1 Stability diagram showing the growth rate ω_i of two-dimensional disturbances as a function of wave number α for the adiabatic-wall case. A weak first-mode instability appears for $\alpha < 1.5$ and a second (Mack) mode for $1.8 < \alpha < 2.6$.

For porous surfaces, we will compare the DNS results with the formulation from Fedorov et al. [5]. Their derivation is not repeated here, but we state the final result for blind pores that the vertical velocity and pressure eigenfunctions at $y = 0$ become linked by the relation

$$\frac{\hat{v}(0)}{\hat{p}(0)} = \frac{n \tanh(-d\sqrt{Z_1 Y_1})}{\sqrt{Z_1/Y_1}} \tag{9}$$

where n is the porosity, d is the pore depth, and the series impedance and shunt admittance are given by

$$Z_1 = \frac{i\omega}{T_w} \frac{J_0(k_v)}{J_2(k_v)} \tag{10}$$

and

$$Y_1 = -i\omega M^2 \left[\gamma + (\gamma - 1) \frac{J_2(k_t)}{J_0(k_t)} \right] \tag{11}$$

respectively, with

$$k_v = r \sqrt{\frac{i\omega \rho_w Re}{\mu_w}} \tag{12}$$

and $k_t = k_v Pr^{0.5}$. The pores are taken to be circular with radius r, J_0 and J_2 denote Bessel functions of the first kind, subscript w refers to conditions at the wall, and all variables are normalized with respect to freestream values, with a reference length given by the displacement thickness of the boundary layer.

Because ω appears as a parameter in the porous-wall formulation and as the result in temporal stability theory, an iterative approach was used until ω_i converged to a specified tolerance (10^{-5}). The thermal admittance was found to have a negligible effect (less than 1%) on the growth rates, as shown by Fedorov et al. [5], and is ignored in the present work.

C. Validation for a Smooth Wall

The first case considered is a smooth-wall boundary layer that develops a Mack mode of instability. The base flow parameters are as described in the previous section. The two-dimensional Mack-mode wavelength is chosen as 3 times the displacement thickness, giving a streamwise wave number of $\alpha = 2\pi/3$. From Fig. 1, it can be seen that the chosen wave number puts this wave near the peak growth rate of the second mode. The linear stability eigenvalue for this case is $\omega = 1.954999 + i0.034134$.

A DNS of this case was set up using 32 points in the streamwise x direction and 401 points in the wall-normal y direction, in which the

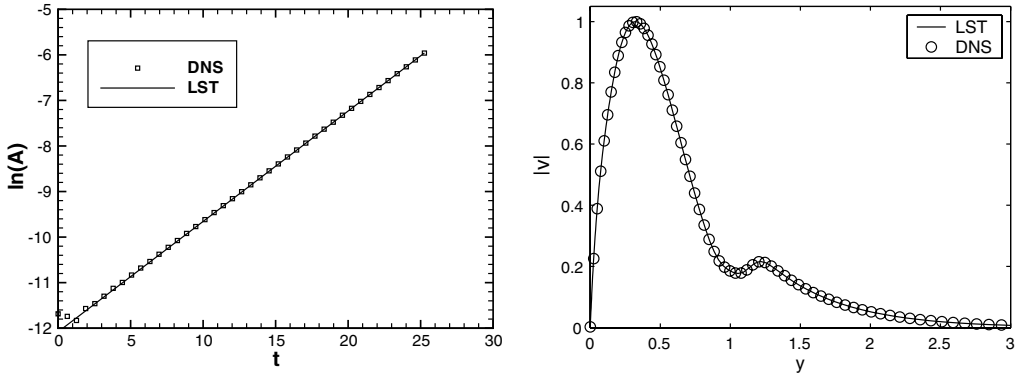

Fig. 2 Smooth-wall validation case of a Mack mode developing in an $M = 6$ and $Re = 20,000$ boundary layer with $T_w = T_{aw}$: a) comparing direct numerical simulation ($N_x = 32$ and $N_y = 401$) values of disturbance amplitude (symbols) with linear stability theory growth rate (solid line) and b) comparing eigenfunction shape at $t = 25.3$.

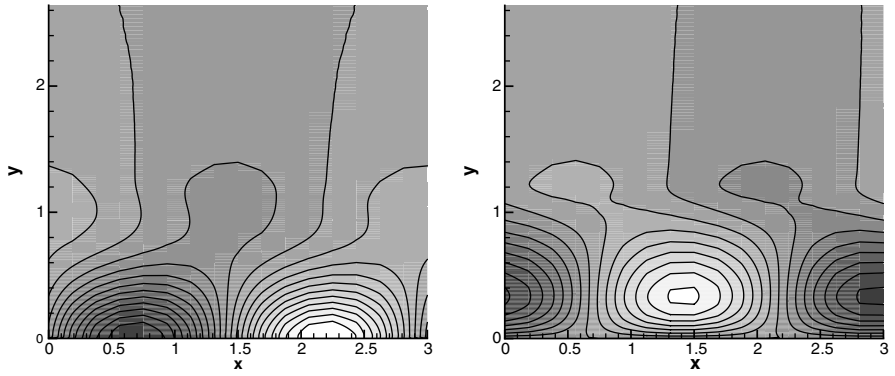

Fig. 3 Mack mode developing above a smooth surface in an $M = 6$ and $Re = 20,000$ boundary layer with $T_w = T_{aw}$: a) contours of pressure and b) contours of normal velocity.

grid was stretched with a coefficient $c = 2.5$ in Eq. (7). The DNS is initialized with an artificial disturbance at $t = 0$ and the eigenmode is allowed to develop from this. The initial disturbance is given by

$$v = 0.0001 \exp[-4(y - 0.8)^2] \sin(2\pi x/L_x) \tag{13}$$

with other variables initialized to the base flow condition. Figure 2a shows the development of the natural logarithm of the root mean square of the v perturbations (integrated over the y direction) as the simulation proceeds. The domain length was chosen as $L_y = 8$ for this test. By $t = 2$ the unstable mode has emerged and grows strongly over the remainder of the simulation. The slope of the solid line is the growth rate from linear stability theory, adjusted for the freestream velocity from the simulations (note that under the FLOWer normalization, the freestream velocity is $M\sqrt{\gamma}$). The agreement for the growth rate is within 0.5%. Grid and domain size tests showed that reducing the grid resolution by a factor of 2 and reducing the domain size to $L_y = 5$ still kept the error less than 2%. The eigenfunction shape is compared in Fig. 2b, showing good agreement between linear stability theory and DNS. Figure 3 shows the developed flowfield for the Mack mode. It can be seen that the largest pressure perturbations are at the wall and the largest normal-velocity fluctuations are at $y = 0.3$. The same test case has been run successfully using the Southampton SBLI code.

III. Mack Mode Stabilization by Spanwise Grooves

In this section, we present results from a set of two-dimensional simulations that explore the influence of the depth and number of pores on the growth rate of the Mack mode from the previous section. Because the simulations are two-dimensional, the porous surface in this case reduces to spanwise grooves. The porosity is kept constant at $n = 0.25$ and the grooves have parallel sides and a depth d. Fedorov et al. [5] suggested that 10–20 pores per wavelength are optimal and we consider cases with number of pores $n_p = 8$ and 16 (smaller number of grooves are of interest to determine whether roughness-induced transition mechanisms are present).

In total, five simulations with spanwise grooves were run: four to cover the effect of number and depth of the grooves ($n_p = 8$ and 16 and $d = 0.3$ and 1.0) and one to study the effect of grid refinement, as listed in Table 1. It turns out that the results are not sensitive to the streamwise grid resolution, and the number of points across the grooves N_g can be chosen as the minimum possible, which is $N_g = 6$ for the present high-order method. For $n = 0.25$, this means that $3N_g = 18$ points are needed between grooves (assuming a uniform grid), and the total grid requirement in the streamwise direction is $N_x = 24n_p$. The simulations were run with the number of points for $y > 0$ set to $N_{y>0} = 251$ and $L_y = 5$, which is a slightly smaller domain, but with a comparable grid density near the surface, compared with the validation case in the previous section. The number of points within the pores is $N_{y<0} = 102$ for $d = 1.0$ and $N_{y<0} = 36$ for $d = 0.3$. Figure 4 shows an example of the growth history for the case with 8 spanwise grooves of depth $d = 1.0$. The penultimate column in Table 1 shows the growth rate ω_i extracted from the simulations and normalized by freestream velocity and displacement thickness.

Table 1 Simulations for cases with spanwise grooves

n_p	d	N_g	ω_i	ω_i (% of smooth-wall case)
8	0.3	6	0.0128	37.3
8	1.0	6	0.0175	51.0
16	0.3	6	0.0245	71.4
16	1.0	6	0.0248	72.2
8	0.3	12	0.0129	37.6

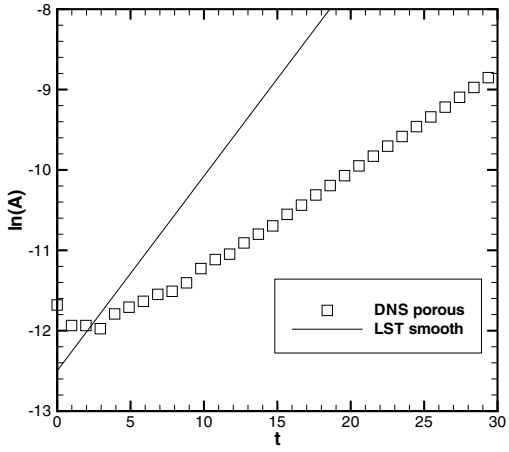

Fig. 4 Mack mode developing above a porous surface (porosity $n = 0.25$, number of pores $n_p = 8$, and pore depth $d = 1.0$) in an $M = 6$ and $Re = 20,000$ boundary layer with $T_w = T_{aw}$, comparing direct numerical simulation ($N_p = 6$ and $N_{y>0} = 251$) values of $\log(v_{\text{rms}})$ (symbols) with the smooth-surface linear stability theory growth rate (solid line).

With groove depth set to $d = 1.0$, Fig. 5 shows pressure (left-hand side) and normal velocity (right-hand side) for 8 grooves (top) and 16 grooves (bottom). It can be seen that in both cases, a Mack mode with a structure similar to the validation case of the previous section has emerged. For 8 grooves, the growth rate is 51.0% of the smooth-wall case, and for 16 grooves, it is 72.2%. Thus, the growth rates are substantially lower than for the smooth-wall case, with higher reductions for fewer grooves. The reasons for this are evident from Fig. 5, in which there is clear flow activity within the grooves. A trailing leg of alternate low and high pressure and positive and negative normal velocity moves within the grooves as the Mack mode passes above. Within the groove, the pressure contours are close to horizontal and the normal velocity is locally parabolic, reducing to

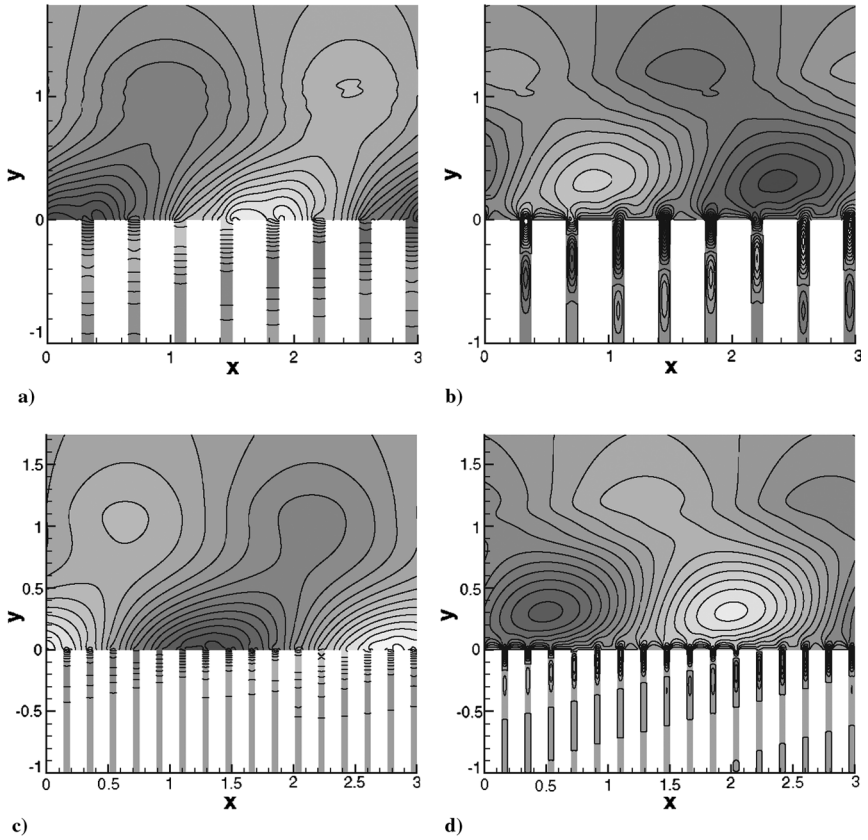

Fig. 5 Mack mode developing above a porous surface (porosity $n = 0.25$ and pore depth $d = 1.0$): a–b) contours of p and v, respectively, for $n_p = 8$ and c–d) contours of p and v, respectively, for $n_p = 16$.

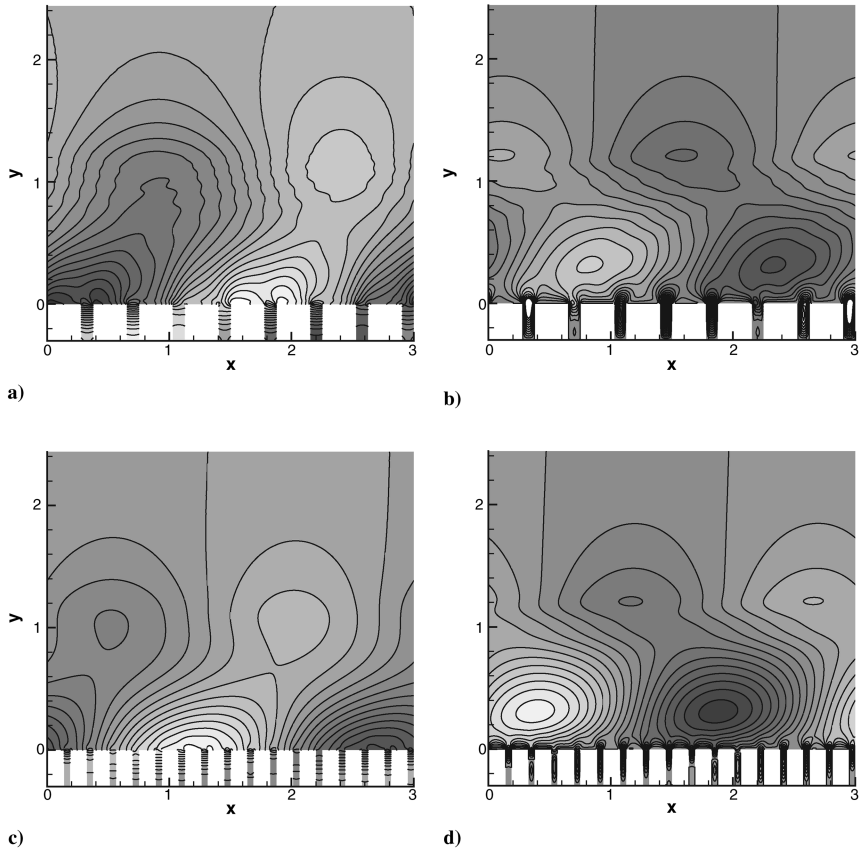

Fig. 6 Mack mode developing above a porous surface (porosity $n = 0.25$ and pore depth $d = 0.3$): a–b) contours of p and v, respectively, for $n_p = 8$ and c–d) contours of p and v, respectively, for $n_p = 16$.

Table 2 Simulations for 3-D cases, all with $d = 1$ and the same hydraulic diameter $d_h = 0.1875$

n_p	Pore length	Pore width	ω_i	L_x	L_z
1	1.5	0.1	0.0179	3.0	0.2
4	0.375	0.125	0.0170	3.0	0.25
8	0.1875	0.1875	0.0165	3.0	0.375

zero on the groove walls to satisfy the no-slip condition. Departures from this pattern are only seen right at the top of the grooves, in which the flow is more clearly two-dimensional. The Mack mode is seen to be superimposed with some high-frequency content, particularly for the 8-groove case (Fig. 5a). This is not a numerical resolution effect, but is caused by sound waves emanating from the groove corners. These waves are of larger amplitude when the grooves are wider. A similar scattering process was observed in [11] when the acoustic absorption properties of a porous surface were studied.

A corresponding set of results for groove depth $d = 0.3$ is shown in Fig. 6, with growth rates given in Table 1. For these shallower grooves, the pattern of flow is complicated by the reflections from the bottom of the groove. Overall, the visualizations are similar to the deeper groove cases shown in Fig. 3. The same high-frequency corruption of the Mack modes is seen for the 8-groove case. Growth rates for these cases are shown in Table 1. For $d = 0.3$ and $n_p = 8$, the growth rate shows the largest reductions of any of the cases studied. For $n_p = 16$, the growth rates are similar for shallow and deep pores.

The last row of Table 1 lists a case for which the streamwise grid resolution was doubled, so that 12 points are across each groove with a total number of points $N_x = 384$. The growth rate in this case is only

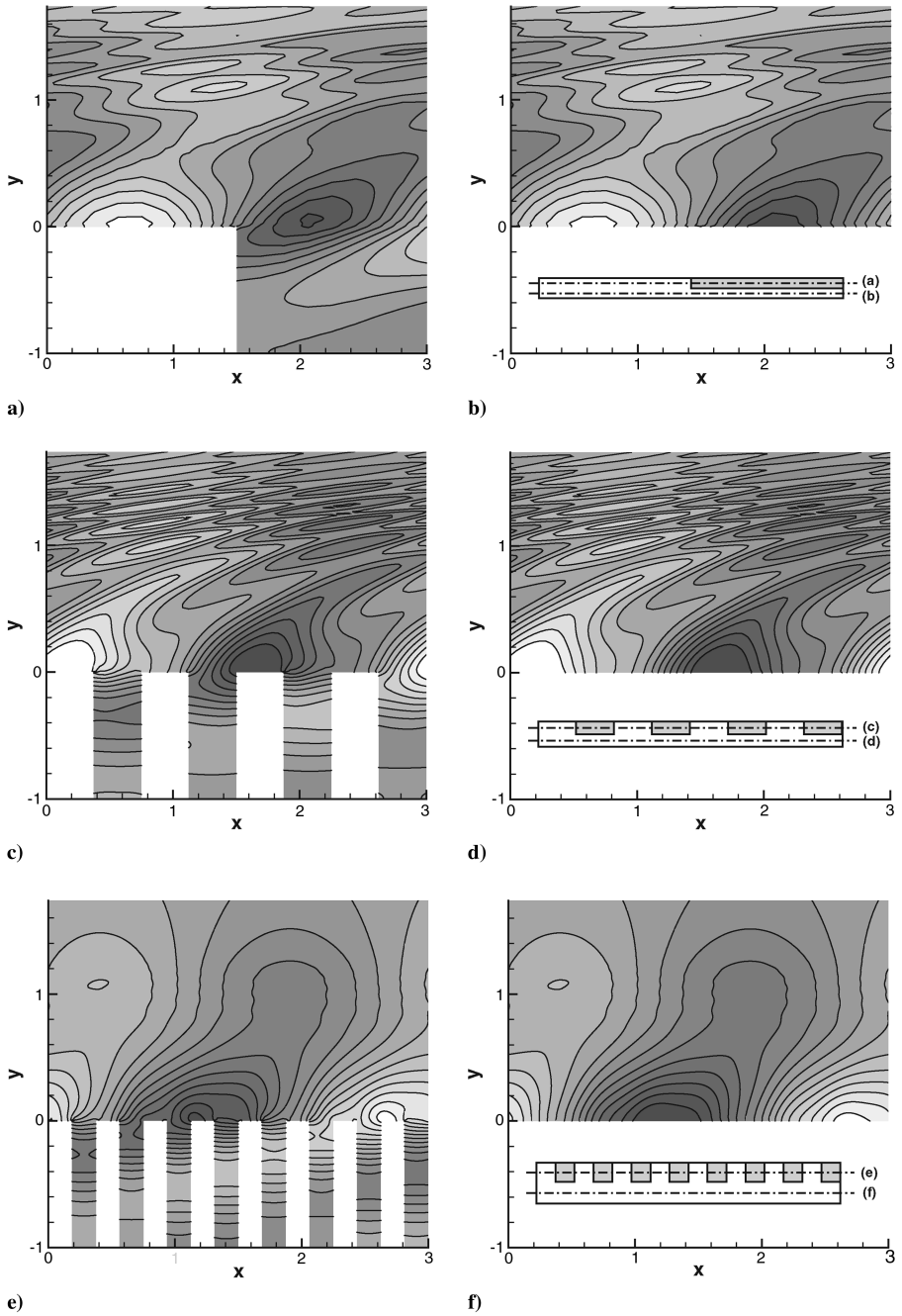

Fig. 7 Mack mode developing above a 3-D porous surface (porosity $n = 0.25$ and pore depth $d = 1.0$). From the top downward, the figures show pressure contours for the number of pores $n_p = 1, 4$, and 8. The left-hand plot in each case is for a plane that cuts through the pores and the right-hand plot is for a spanwise location that avoids the pores, shown by the insets as a top view with pores in gray.

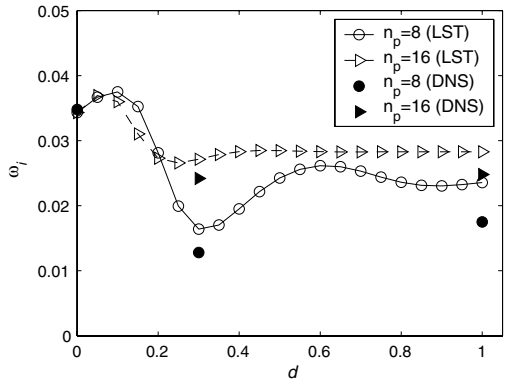

Fig. 8 Comparison of LST of porous surfaces (lines) with DNS (filled symbols) at $M = 6$, fixed wall temperature $T_w = Taw$, and $Re = 20,000$. Porous surface with $n = 0.25$, simulations with $N_p = 6$, $N_y = 251$, and stretching factor $c = 2.5$.

1.2% different from the original case, suggesting that the results are not very sensitive to the grid. The simplicity of the flow within the pores (uniform pressure and parabolic normal velocity) also supports this conclusion.

IV. Simulations with Three-Dimensional Pores

Table 2 shows a list of three-dimensional simulations that were run to check the effect of pore shape. All of the cases have a depth $d = 1.0$ and the same hydraulic diameter $d_h = 0.1875$, defined as

$$d_h = \frac{4A_p}{C} \tag{14}$$

where A_p is the pore area and C is the circumference. The hydraulic diameter was suggested by Fedorov et al. [8] as a method for comparing pores with different structures. The equivalent two-dimensional case was the one with $n_p = 8$. The three-dimensional cases are for numbers of pores over one wavelength $n_p = 1, 4$, and 8. The first corresponds to narrow streamwise slots with an aspect ratio of 15, and the last corresponds to square pores.

For each of the cases, Fig. 7 shows two slices through the flowfield: one slice at a spanwise location that passes through the pores and the other for a spanwise location at which there are no pores. For $y > 0$, the results are almost identical, showing that the instability mode remains two-dimensional. For $n_p = 1$, the disturbance to the flow caused by the slot is large. Each time the pressure perturbations of the Mack mode pass over a sharp corner at the leading and trailing edges of the slot, a sound wave is generated. This propagates downstream and outward and, due to the periodic boundary condition, appears as a series of waves in the wall-normal direction. Comparable plots for the cases $n_p = 4$ and 8 are also shown in Figs. 7c–7f. The regular emission of sound waves can be clearly seen for $n_p = 4$, whereas the $n_p = 8$ case is much smoother. As in the two-dimensional simulations, the disturbances caused by the pores reduce in amplitude as the number of pores is increased. In each case, the flow outside the pores is still closely two-dimensional.

Growth rates for the three-dimensional cases are shown in Table 2 and can also be compared with the $n_p = 8$ case in Table 1, which had $\omega_i = 0.0175$. It can be seen that there is a very slight increase in the effectiveness of the porosity in reducing the growth rate as the pore shape moves toward the square configuration ($n_p = 8$). The square pore case is 8% more effective than the streamwise slot case, for example. However, these changes are small and the main conclusion is that the hydraulic diameter does a good job of collapsing the data for pores with quite different shapes. The base flow slip discussed in Sec. II.A remains small for all the cases studied, being of the order of 0.1% of the freestream velocity.

V. Comparison with Stability Theory

To compare with linear stability theory (LST), we take the pore radius in the stability theory to be $r = 0.5d_h$, where the hydraulic diameter d_h is defined by Eq. (14). For spanwise grooves, the radius is equal to the groove width, whereas for square pores, the appropriate radius is half the length of the sides.

A comparison of LST with DNS for spanwise grooves is shown in Fig. 8, in which growth rate ω_i is plotted as a function of pore depth. For the present configuration with $n_p = 8$, there is a continuing effect of pore depth up to $d = 1$, in contrast to Fedorov et al. [5], for which the example case leveled off for $d > 0.3$. Pores with a larger radius apparently have to be deeper to get to the asymptotic deep-pore condition. It can be seen that the growth rates from DNS (the solid symbols) are below those from LST, implying a stronger damping due to porosity when the pores are resolved. A similar underprediction of the effect of porosity is shown by Maslov [7] (see Fig. III.40); however, the data published by Fedorov et al. [8] suggest a large degree of uncertainty in the comparisons, with important nonparallel effects. Note that in the present work, we are comparing like with like, because the DNS base flow is forced to be parallel, matching the LST assumption.

VI. Simulations with Cold Walls

Because hypersonic wind-tunnel tests are usually carried out in blowdown facilities in which the measurement time is too short to increase the wall temperature significantly, DNS simulations with a low constant wall temperature were carried out. The wall temperature was chosen with $T_w = 1.2 \cdot T_\infty$ with a reference temperature of $T_\infty = 216.65$ K, as used in the previous cases. Because the viscosity for this case changed strongly with the chosen wall temperature, the

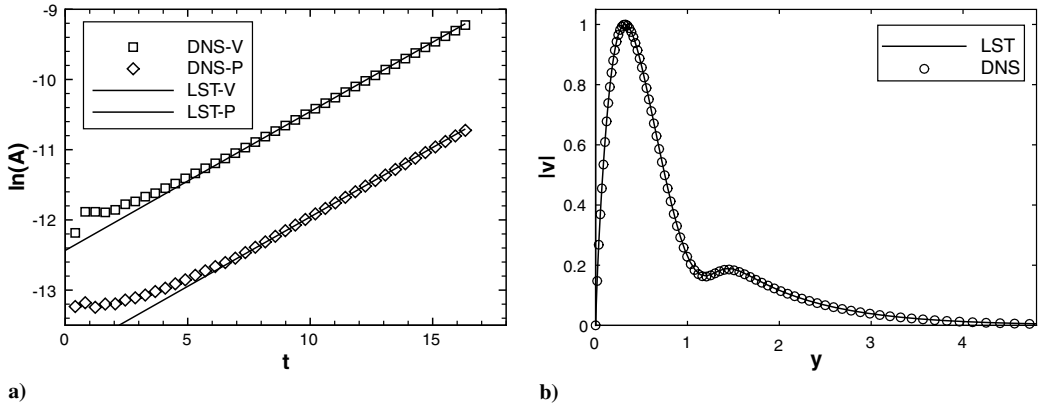

Fig. 9 Smooth-wall validation case of a Mack mode developing in an $M = 6$ and $Re = 6000$ boundary layer with $T_w = 1.2 \cdot T_\infty$: a) comparing direct numerical simulation ($N_x = 32$ and $N_y = 401$) values of disturbance amplitude (symbols) with linear stability theory growth rate (solid line) and b) comparing eigenfunction shape.

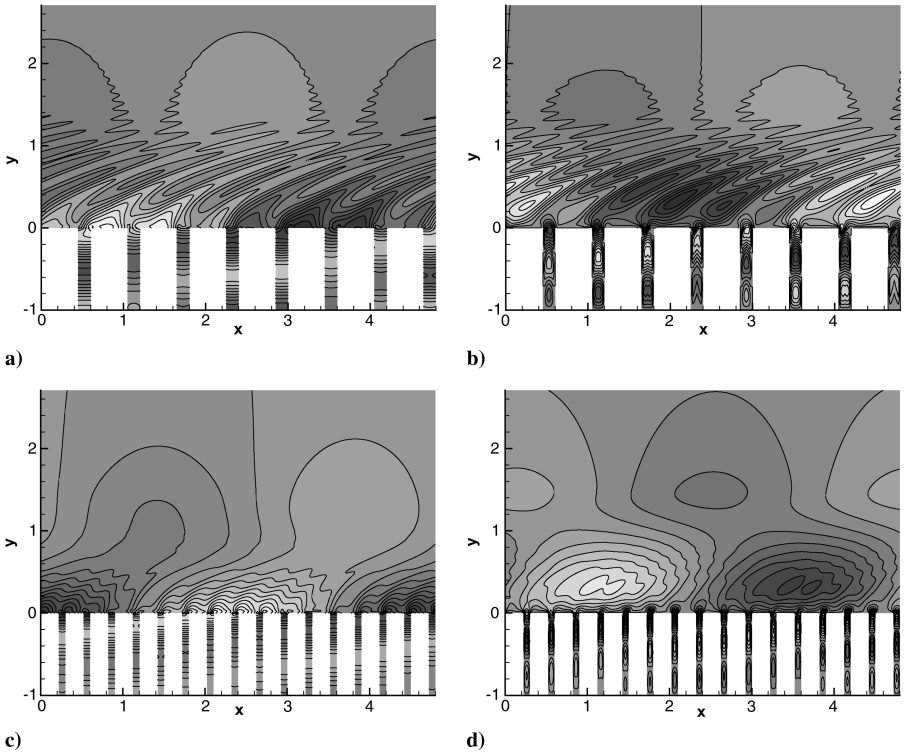

Fig. 10 Mack mode developing above a porous surface with $n = 0.25$ porosity and pore depth $d = 1.0$ at $M = 6$, $Re = 6000$, and $T_w = 1.2 \cdot T_\infty$: a–b) contours of p and v, respectively, for $n_p = 8$ and c–d) contours of p and v, respectively, for $n_p = 16$.

Reynolds number was reduced to $Re = 6000$. Under these conditions, a finer grid in the near-wall boundary layer was necessary and, consequently, the number of wall-normal points was increased to 401, whereas the number of points in the x direction was the same as for equivalent hot-wall cases. The wavelength of the peak growth rate also changes. The linear stability eigenvalue for this case is $\omega = 1.187048 + i0.027849$, and so the streamwise wave number is chosen as $\alpha = 2\pi/4.8$, which is a wavelength of 4.8 times the displacement thickness. For these simulations the domain size was set to $L_x = 4.8$ and $L_y = 8$.

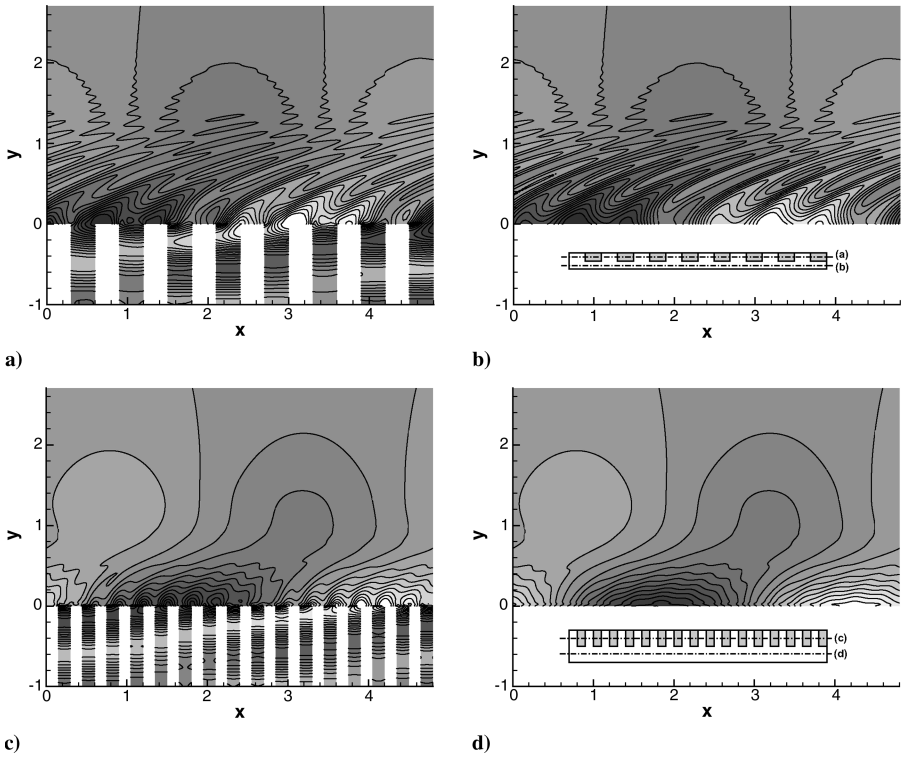

Fig. 11 Mack mode developing above a 3-D porous surface (porosity $n = 0.25$ and pore depth $d = 1.0$) at $M = 6$, $Re = 6000$, and $T_w = 1.2 \cdot T_\infty$. The figures show pressure contours for 8 and 16 pores (top and bottom). The left-hand plot in each case is for a plane that cuts through the pores and the right-hand plot is for a spanwise location that avoids the pores, shown by the insets as a top view with pores in gray.

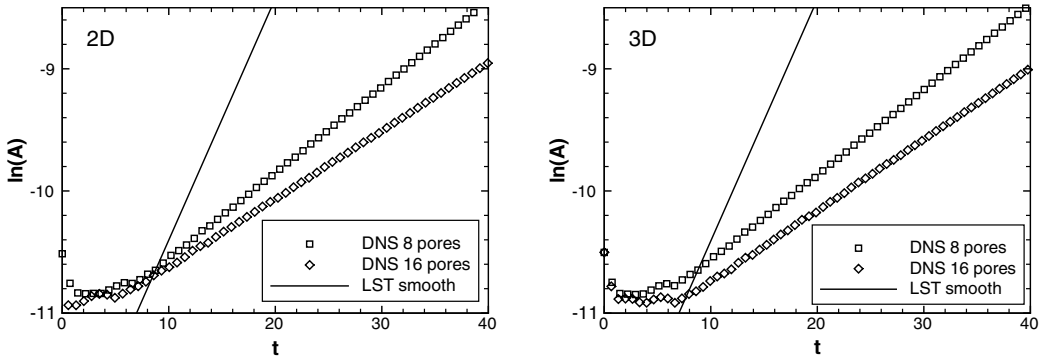

Fig. 12 Mack mode developing above a 3-D porous surface (porosity $n = 0.25$, pore depth $d = 1.0$) at $M = 6$, $Re = 6000$, and $T_w = 1.2 \cdot T_\infty$. Comparison of direct numerical simulation values of $\log(v_{\text{rms}})$ (symbols for 8 and 16 pores) with the smooth-surface linear stability theory growth rate (solid line): a) two-dimensional simulations and b) three-dimensional simulations.

To validate these calculations in the same way as the cases with an adiabatic wall, they were compared with LST results, as shown in Fig. 9. For these conditions, the unstable mode emerges by $t = 8$, which is later than for adiabatic-wall cases. Afterward, it grows with the same rate as the LST results with an error of less than 2%.

Two-dimensional simulations of 8 and 16 pores with a groove depth of $d = 1.0$ are carried out for the same porosity of $n = 0.25$ as in the former tests. Figure 10 shows pressure and normal-velocity distribution for both cases. In comparison with the adiabatic-wall case of Fig. 5, the high-frequency content, described in Sec. III, is stronger due to the larger diameter of the pores that results from the increased wavelength at constant porosity. In fact, the pressure distribution of the 8-pore case in Fig. 10a is comparable with Fig. 7c with only four pores. Consequently, the 16-pore simulation is also superimposed by a strong high-frequency content. Pressure contours for three-dimensional pores with the same wall temperature and flow conditions described before are shown in Fig. 11. Again, the hydraulic diameter is kept constant at $d_h = 0.2$, with rectangular lengthwise or crosswise pores for 8 or 16 pores, respectively. Both results show the same behavior already described for the adiabatic results. Sound waves are generated as the pressure perturbations of the Mack mode pass a sharp corner and, especially for 8 pores, the sound waves propagating outward are clearly visible. The two-dimensionality of the flow outside the pores is also seen, as mentioned for the adiabatic-wall results. The growth history of the wall normal-velocity component for the 8- and 16-pore simulations of spanwise grooves and three-dimensional pores is shown in Fig. 12. The unstable mode has emerged by $t = 10$ and shows exponential growth with a similar growth rate for grooves and pores of the same extent. For all porous cases, the growth rate is strongly reduced in comparison with the LST result of the smooth wall. The growth rates are shown in Table 3 for two- and three-dimensional simulations, given by the value of "dim" in the second column. The tendency of decreasing growth rates with increasing pore numbers is the same for grooves and pores, consistent with the changes seen earlier for three-dimensional cases with adiabatic walls (see Fig. 11a). Similar results have also been observed for cases with irregular pore distributions, indicating that the behavior is not limited to regular arrays of pores.

Table 3 Simulations for cases with constant low wall temperature

n_p	dim[a]	ω_i	ω_i (% of smooth-wall case)
8	2	0.00983	35.2
16	2	0.00822	29.5
8	3	0.00991	35.6
16	3	0.00785	28.2

[a]Spanwise grooves are dim = 2 and three-dimensional pores are dim = 3.

VII. Conclusions

A direct numerical simulation approach has been used to study hypersonic flow over a porous surface, in which the individual pores are resolved on the computational grid. The code was validated by calculation of a Mack mode of instability in a boundary layer under a stream at Mach 6 over a smooth wall, with a fixed wall temperature equal to the adiabatic-wall temperature. In addition, two and three-dimensional calculations with cold walls at a lower Reynolds number of 6000 have been carried out. Results for two- and three-dimensional simulations of rectangular porous surfaces demonstrate strong stabilization of the Mack mode of instability. Except near the region of entry to the pore, the flow within the pores is unidirectional to a good approximation, supporting one of the main assumptions made in the linear stability theory. The stabilizing effect is found to be generally stronger than predictions from the linear stability model, with growth rates 10–30% smaller, depending on porosity and pore depth. Pore shape does not seem to be a large factor: spanwise grooves, streamwise slots, and square pores all give similar growth rates for the same hydraulic diameter of the pores.

For the particular conditions studied here, the Knudsen number is of the order of 0.01 to 0.1, putting the flow cases strictly into the slip regime. This regime was studied by Maslov [7], who showed linear calculations for a Knudsen number of 0.588 having a 15–20% reduced growth rate for porous surfaces. At the Knudsen numbers for the present study, the effect is therefore likely to be small. It is important that both increasing Knudsen number and increasing realism of the pore representation both show reduced growth rate of the Mack mode of instability.

The mechanism of final breakdown to turbulence has not been considered here. It is planned to run further simulations to study secondary instability and interactions with the most unstable oblique first mode. With respect to a possible "roughness" type of transition caused by large pores, the present study has noted the increasing amplitude of sound waves generated by the interaction of Mack modes with pore corners as the pore size is increased. Such disturbances may feed other instability processes in the flow, but the precise mechanism remains to be studied.

Appendix: Nonuniqueness of Compressible Orr–Sommerfeld Solutions

When comparing eigenvalues between DNS and Orr–Sommerfeld solutions for compressible flows, we need to be aware that the solutions may depend on the formulation of the equations. To see this, we start from the Navier–Stokes equations, given in conservative formulation by Eqs. (1–3). An equivalent set of equations for primitive variables may be derived by subtracting u_i times Eq. (1) from Eq. (2) and subtracting u_i times the resulting momentum equation and e times Eq. (1) from Eq. (3). This leads to

$$\frac{\partial \rho}{\partial t} + u_j \frac{\partial \rho}{\partial x_j} + \rho \frac{\partial u_j}{\partial x_j} = 0 \tag{A1}$$

$$\rho \frac{\partial u_i}{\partial t} + \rho u_j \frac{\partial u_i}{\partial x_j} + \frac{\partial p}{\partial x_i} = \frac{\partial \tau_{ij}}{\partial x_j} + f_i \tag{A2}$$

$$\rho \frac{\partial e}{\partial t} + \rho u_j \frac{\partial e}{\partial x_j} + p \frac{\partial u_i}{\partial x_i} = -\frac{\partial q_i}{\partial x_i} + \tau_{ij} \frac{\partial u_i}{\partial x_j} + g - u_i f_i \tag{A3}$$

The forcing term in the energy equation would have to be $h = g - \bar{u}_i f_i$ to maintain the steady base flow. A slight difference therefore emerges when we linearize the equations, because Eq. (A3) will give a term $u_i' f_i$, which would not have been present had we just used the forcing term h. The difference only occurs in the energy equation and consists of the term

$$u' f_x = u' \left(\bar{\mu} \frac{d^2 \bar{u}}{dy^2} + \frac{d\bar{\mu}}{dy} \frac{d\bar{u}}{dy} \right) \tag{A4}$$

This term would disappear for base flows that exactly satisfy the steady momentum equation.

The differences are not just an artifact of the forcing that would be used in a DNS to maintain a parallel base flow. When a linearized energy equation is derived from Eq. (3) without the forcing terms, it contains the terms in Eq. (A4), whereas if the equation is derived from Eq. (A3), it does not contain these terms.

As an example, consider a perfect-gas Mach 6 boundary layer with an adiabatic no-slip wall boundary condition at $Re = 20,000$, $Pr = 0.72$, and $\gamma = 1.4$, with Sutherland's law constant of 110.4 K and a reference temperature of 216.65 K. A Mack mode with wavelength equal to three displacement thicknesses is considered, with disturbance temperature and velocity set to zero at the wall. Temporal stability analysis from the primitive variable formulation gives a growth rate of $\omega_i = 0.034013$, whereas the conservative formulation gives $\omega_i = 0.034134$. In practical calculations, the differences are likely to remain small, but it is surprising to find any differences at all. For unique solutions, one would need a consistent treatment of nonparallel terms to uniform order, as is done, for example, in the parabolized stability equations framework [16].

Acknowledgments

This work was carried out while the first author was a guest scientist at DLR, German Aerospace Center, in Braunschweig. The authors would like to acknowledge the support received from J. Longo and C.-C. Rossow in setting up this visit.

References

[1] Liepmann, H. W., and Nosenchuck, D. M., "Active Control of Laminar-Turbulent Transition," *Journal of Fluid Mechanics*, Vol. 118, 1982, pp. 201–204. doi:10.1017/S0022112082001037

[2] Gad-el-Hak, M., *Flow Control: Passive, Active and Reactive Flow Management*, Cambridge Univ. Press, Cambridge, MA, 2007.

[3] Carpenter, P. W., and Porter, L. J., "Effects of Passive Porous Walls on Boundary-Layer Instability," *AIAA Journal*, Vol. 39, No. 4, 2001, pp. 597–604. doi:10.2514/2.1381

[4] Mack, L. M., "Boundary Layer Linear Stability Theory," AGARD Rept. 709, Neuilly-sur-Seine, France, 1984.

[5] Fedorov, A. V., Malmuth, N. D., Rasheed, A., and Hornung, H. G., "Stabilization of Hypersonic Boundary Layers by Porous Coatings," *AIAA Journal*, Vol. 39 No. 4, 2001, pp. 605–610. doi:10.2514/2.1382

[6] Rasheed, A., Hornung, H. G., Fedorov, A. V., and Malmuth, N. D., "Experiments on Passive Hypervelocity Boundary-Layer Control Using an Ultrasonically Absorptive Surface," *AIAA Journal*, Vol. 40, No. 3, 2002, pp. 481–489. doi:10.2514/2.1671

[7] Maslov, A. A., "Experimental and Theoretical Studies of Hypersonic Laminar Flow Control Using Ultrasonically Absorptive Coatings (UAC)," International Science and Technology Center, Rept. 2172-2001, Moscow, May 2003.

[8] Fedorov, A., Shiplyuk, A., Maslov, A., Burov, E., and Malmuth, N., "Stabilization of a Hypersonic Boundary Layer Using an Ultrasonically Absorptive Coating," *Journal of Fluid Mechanics*, Vol. 479, 2003, pp. 99–124. doi:10.1017/S0022112002003440

[9] Chokani, N., Bountin, D. A., Shiplyuk, A. N., and Maslov, A. A., "Nonlinear Aspects of Hypersonic Boundary Layer Stability On A Porous Surface," *AIAA Journal*, Vol. 43, No. 1, 2005, pp. 149–155. doi:10.2514/1.9547

[10] Egorov, I. V., Fedorov, A. V., Novikov, A. V., and Soudakov, V. G., "Direct Numerical Simulation of Supersonic Boundary-Layer Stabilization by Porous Coatings," AIAA Paper 2007-948, 2007.

[11] Bres, G. A., Colonius, T., and Fedorov, A. V., "Interaction of Acoustic Disturbances with Micro-Cavities for Ultrasonic Absorptive Coatings," 5th AIAA Theoretical Fluid Mechanics Conference, AIAA Paper 2008-3903, Seattle, WA, 23–26 June 2008.

[12] Bres, G. A., Colonius, T., and Fedorov, A. V., "Stability of Temporally-Evolving Supersonic Boundary Layers over Micro-Cavities for Ultrasonic Absorptive Coatings," 5th AIAA Theoretical Fluid Mechanics Conference, AIAA Paper 2008-4337, Seattle, WA, 23–26 June 2008.

[13] Enk, S., "A Fourth Order Finite Difference Method for Large Eddy Simulation at a Flat Plate," *Notes on Numerical Fluid Mechanics and Multidisciplinary Design* (to be published).

[14] Kroll, N., and Jain, R. K., "Solution of Two-Dimensional Euler Equations- Experience with a Finite Volume Code," DFVLR Forschungsbericht, Rept. 87-41, Braunschweig, Germany, 1987.

[15] Malik, M. R., "Numerical Methods for Hypersonic Boundary Layer Stability," *Journal of Computational Physics*, Vol. 86, No. 2, 1990, pp. 376–413. doi:10.1016/0021-9991(90)90106-B

[16] Herbert, T., "Parabolized Stability Equations," *Annual Review of Fluid Mechanics*, Vol. 29, 1997, pp. 245–283. doi:10.1146/annurev.fluid.29.1.245

A. Tumin
Associate Editor